

See discussions, stats, and author profiles for this publication at: <https://www.researchgate.net/publication/260215091>

# Calculation of Iron Transport through Human H-chain Ferritin

ARTICLE *in* THE JOURNAL OF PHYSICAL CHEMISTRY A · FEBRUARY 2014

Impact Factor: 2.69 · DOI: 10.1021/jp500198u · Source: PubMed

---

CITATIONS

2

---

READS

66

## 4 AUTHORS, INCLUDING:



Rozita Laghaei

Pittsburgh Supercomputing Center

22 PUBLICATIONS 379 CITATIONS

[SEE PROFILE](#)



William j Kowallis

Carlow University

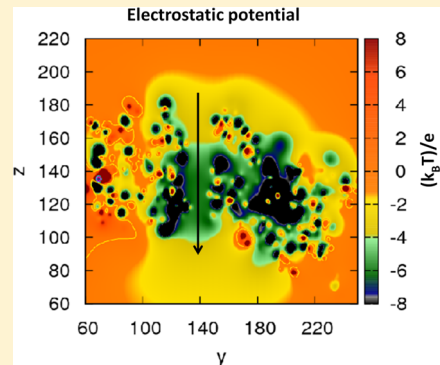
3 PUBLICATIONS 50 CITATIONS

[SEE PROFILE](#)

# Calculation of Iron Transport through Human H-chain Ferritin

Rozita Laghaei,<sup>†</sup> William Kowallis,<sup>‡</sup> Deborah G. Evans,<sup>§</sup> and Rob D. Coalson\*,<sup>†</sup><sup>†</sup>Department of Chemistry, University of Pittsburgh, Pittsburgh, Pennsylvania 15260, United States<sup>‡</sup>Department of Chemistry, Carlow University, Pittsburgh, Pennsylvania 15213, United States<sup>§</sup>The Nanoscience and Microsystems Program and the Department of Chemistry and Chemical Biology, University of New Mexico, Albuquerque, New Mexico 87131-0001, United States

**ABSTRACT:** Influx of ferrous ions from the cytoplasm through 3-fold pores in the shell of ferritin protein is computed using a 3-dimensional Poisson–Nernst–Planck electrodiffusion model, with inputs such as the pore structure and the diffusivity profile of permeant  $\text{Fe}^{2+}$  ions extracted from all-atom molecular dynamics (MD) simulations. These calculations successfully reproduce experimental estimates of the transit time of  $\text{Fe}^{2+}$  through the ferritin coat, which is on the millisecond time scale and hence much too long to be directly simulated via all-atom MD. This is also much longer than the typical time scale for ion transit in standard membrane spanning ion channels whose pores bear structural similarity to that of the 3-fold ferritin pore. The slow time scale for  $\text{Fe}^{2+}$  transport through ferritin pores is traced to two features that distinguish the ferritin pore system from standard ion channels, namely, (i) very low concentration of cytoplasmic  $\text{Fe}^{2+}$  under physiological conditions and (ii) very small internal diffusion coefficients for ions inside the ferritin pore resulting from factors that include the divalent nature of  $\text{Fe}^{2+}$  and two rings of negatively charged amino acids surrounding a narrow geometric obstruction within the ferritin pore interior.



## 1. INTRODUCTION

Ferritins play a central role in iron storage in most forms of life, ranging from vertebrates through plants to microorganisms.<sup>1</sup> They control iron levels in organisms through the sequestration and release of iron from hydrated ferric oxide minerals stored in their inner cavity<sup>2</sup> and protect the cell against oxidative stresses.<sup>3–8</sup> Iron homeostasis and regulation is essential because iron is required in many cellular redox processes and electron transfer reactions. However, in high concentrations, iron can react to form toxic radicals and other chemical species,<sup>9</sup> and consequently its activity in cells needs to be strictly regulated.

Ferritins *in vitro* have also been used for several materials science<sup>10</sup> and biomedical applications.<sup>11</sup> Ferritins have been successfully used to synthesize nanoparticles using a variety of metals, e.g., Au, Ag, Pt, Co, Cr, and Zn.<sup>12–14</sup> Wild-type and mutant ferritin nanocages allows for the synthesis of monodisperse nanoparticles less than 8 nm in diameter and often incorporating novel mineral types.<sup>12,15–19</sup> Given the ability for bioassembly onto surfaces, ferritin can be used to create ordered arrays of paramagnetic nanoparticles with applications in the computer industry.<sup>20–22</sup> Ferritins have also been used as delivery vehicles for diagnostic and therapeutic agents.<sup>11</sup> Recent research on nanobatteries based on the ferritin structure has clearly demonstrated the potential for using ferritins for novel nanoscale applications.<sup>23,24</sup>

Mammalian ferritins have a nearly spherical shell-like structure, with 432 octahedral symmetry, and are composed of 24 subunits.<sup>25,26</sup> The subunits are comprised of 4- $\alpha$  helix bundles (with an additional fifth short helix at 60° to the bundle), usually of two different types, H (~21 000 Da) and L

(~19 500 Da). Heteropolymers of H- and L-subunits are normally found in mammals, and the ratio of these is tissue specific.<sup>26</sup> The protein coat composed of these assembled subunits is approximately 20 Å thick and surrounds an approximately 80 Å wide central cavity, where iron is stored in mineral form.

The first steps to sequestration of iron as a mineral in the core consist of the uptake of  $\text{Fe}^{2+}$  through the protein and then oxidation to  $\text{Fe}^{3+}$  at the ferroxidase sites. The ferroxidase sites (found only in the H subunits) have been well characterized through a variety of spectroscopic and crystallographic studies.<sup>27,28</sup> The binding sites at the ferroxidase site are composed of highly conserved residues in animal ferritins and are found in the center of the  $\alpha$ -helix bundles of the H-subunits.<sup>5,29</sup> Recently, NMR techniques have been used to elucidate the pathway followed from these ferroxidase sites to incorporation of iron in the biomimetic core.<sup>30</sup>  $\text{Fe}^{3+}\text{O}$  multimers move about 20 Å along the inner core to nucleate at the 4-fold channel openings on the inside of the protein coat before moving to the interior.

The entry of iron ions occurs through eight hydrophilic channels located along the 3-fold axes.<sup>31–33</sup>  $\text{Fe}^{2+}$  enters the pores of these channels created at the vertices of three subunits. These channels are 15–20 Å in length, and exit pores open into

**Special Issue:** Kenneth D. Jordan Festschrift

**Received:** January 7, 2014

**Revised:** February 13, 2014

the internal cavity about 15 Å from the ferroxidase site residues. The hydrophilic channels are highly conserved in animals and are lined with a number of carboxylated residues, notably Glu and Asp. Site specific mutagenesis and crystallographic data point to at least three possible binding sites along the 3-fold channel.<sup>32–35</sup> Crystallographic evidence shows the capture of Zn<sup>2+</sup> (an Fe<sup>2+</sup>-like surrogate) in three specific sites along the 3-fold channels.<sup>36,37</sup> Mutations of the Asp and Glu in the channels of ferritins result in significant changes in the uptake of iron,<sup>35,38</sup> and blocking of the outside pore opening by a [Cr(Tren)(H<sub>2</sub>O)(OH)]<sup>2+</sup> complex<sup>39</sup> or peptides<sup>31</sup> also significantly alters the entry of iron. Opening of the pores by chaotropic agents<sup>40</sup> or site directed mutagenesis<sup>41,42</sup> also leads to increased uptake and effusion of iron. The Asp131 and Glu134 residue structure in human H chain ferritin is highly conserved in animals. The channel is funnel shaped with a negative electrostatic potential on the outer opening and a negative gradient between the outside and the internal portion of the channel.<sup>33,43,44</sup> About halfway down the channel, a triad of E134 residues (one from each subunit making up the 3-fold pore) and a similar triad of D131 residues form the constriction in this funnel-shaped channel. Crystallographic data from a variety of ferritin structures show that these residues are about 5–6 Å apart and form a constriction about 4–5 Å wide in the crystal structure.<sup>33</sup> The hydrated octahedral complex [Fe(H<sub>2</sub>O)<sub>6</sub>]<sup>2+</sup> has a radius of about 5.6 Å,<sup>45</sup> and it is not known whether ligand exchange is required to move iron through the channel. Recent crystallographic studies have identified several hydrated Mg<sup>2+</sup> ions captured in the 3-fold channels near these binding sites.<sup>34,46</sup>

Although crystallographic data, mutagenesis, and spectroscopic studies have elucidated the path of divalent ions into the ferritin structure through the 3-fold channels, the rate of diffusion of iron in these channels is important for understanding the energetics and kinetics involved in uptake of iron.<sup>47</sup> The rate constant for the kinetics of Fe<sup>2+</sup> from solution into the core of ferritin has been measured using horse spleen ferritin.<sup>48</sup> The rate of Fe<sup>2+</sup> penetration was measured spectroscopically by the formation of Prussian Blue in the ferritin core. The rate of reaction of Fe<sup>2+</sup> in solution to form Prussian Blue in the ferritin core evidenced a lag time in comparison to the formation of Prussian Blue in solution. This lag time is indicative of the rate of iron diffusion from solution to the ferritin core. The study concluded that the rate constant from solution to the inner core of ferritin is 0.4 s<sup>-1</sup> and estimated the diffusion constant to be about  $5 \times 10^{-20}$  m<sup>2</sup>/s. A stopped flow fluorescence and absorption study was conducted on a series of fluorescent variants of human H ferritins.<sup>49</sup> These studies were able to demonstrate that the 3-fold and not the 1-fold channels provide Fe<sup>2+</sup> access to the ferritin core. In addition, the rate constant was determined by stopped flow fluorescence quenching data. This rate constant of 216 s<sup>-1</sup> and a half-life of 3 ms is estimated to correspond to the diffusion of iron through the 3-fold channels to the ferroxidase site. An estimate of the apparent diffusion constant in the 3-fold channels from this data is  $5 \times 10^{-16}$  m<sup>2</sup>/s, which is considerably slower than that of the hydrated Fe<sup>2+</sup> ion in solution of  $7 \times 10^{-10}$  m<sup>2</sup>/s.

Neither the crystallographic nor kinetic data can provide a more complete model of the dynamics of migration of iron as it moves through the 3-fold channel. In particular, the effects on the rate of iron diffusion through the channel due to random thermal motion, electrostatic gradients on the protein surface,

and fluctuational changes in the 3-fold channel due to protein motion in solution are not easily extracted. In this regard classical molecular dynamics simulations (MD) can be used to elucidate the dynamics and energetics of an ion permeating through an ion channel. Indeed, a recent classical MD simulation of ferritin in the presence of iron has corroborated previous experimental observations and provided new insight into the dynamics of this process.<sup>50</sup> These molecular dynamics simulations of human H chain ferritin have confirmed that iron enters primarily through the 3-fold channels and that iron binds strongly to the sites created by Asp131 and Glu134 and binds weakly to two other sites around His118 and Cys130, closer to the pore opening. The simulations also indicate a pathway for the iron after exiting the pore on the interior surface to the ferroxidase site through a sequence of residues, namely Thr135, His136, and Tyr137. In addition, these simulations provide dynamical information of how the iron moves through the channels and capture the response of the protein to the ion as it does so. Mechanistically, the simulations suggest that an Fe<sup>2+</sup> ion remains in the three-channel binding sites until displaced by another entering Fe<sup>2+</sup> ion, whereupon the ion closest to the interior exits the channel and moves to the ferroxidase site.

Experiment suggests at least millisecond time scales for  $t_{1/2}$  in the channel under physiological conditions.<sup>49</sup> Given the long time scales involved, classical molecular dynamics cannot be used to determine the rate of permeation in this system. However, Poisson–Nernst–Planck (PNP) theory,<sup>51</sup> which has been shown to provide an efficient and generally effective method of determining transport of ions through standard membrane spanning ion channels,<sup>52</sup> does not rely on explicit dynamical simulation and is thus a more promising candidate for initial investigation of the kinetics of ion flow through 3-fold ferritin pores.

It is the goal of the present study to use the PNP method to obtain an estimate for ion transport rates through the 3-fold channels in ferritin. PNP theory requires as input spatial diffusivity profiles of the permeant ions throughout the pore region. Here we use short-time all-atom simulations to calculate the appropriate diffusivity profiles, and then feed this information into a 3D PNP calculation of Fe<sup>2+</sup> flux through a 3-fold pore. The inverse of the ion current thus extracted is used as an approximate measure of the transit time of a single Fe<sup>2+</sup> ion through the channel. This allows for direct comparison with previous kinetics experiments. Validation obtained by comparing such simulation models to experiment would be extremely useful. With the accuracy of the simulations confirmed, they could be used for future studies of ions other than Fe<sup>2+</sup> permeating through the ferritin structure and for calculating transport rates of other species (even oxo and chloro anions of metals) through the channel.<sup>53</sup> In the case of Fe<sup>2+</sup> ions, these simulations also provide insight into why the diffusion of the ions is so slow compared with the free hydrated ion in solution, and provide a picture of the uptake of iron into ferritin at atomic resolution. The theoretical approach used here provides insight into the different factors effecting transport rates: diffusion, electrostatics, and protein conformation in solution.

## 2. METHODS

### 2.1. Molecular Dynamics Simulation of Ferritin.

Molecular dynamic simulations in the NPT ensemble were performed using the NAMD molecular dynamics (MD) simulation program<sup>54</sup> with the CHARMM22 force field<sup>55</sup> for

the human H-ferritin protein (2FHA), which consists of 24 subunits. Simulations of the three-unit hydrophilic channel forming part of ferritin (Figure 1A, inset) comprising 50 465

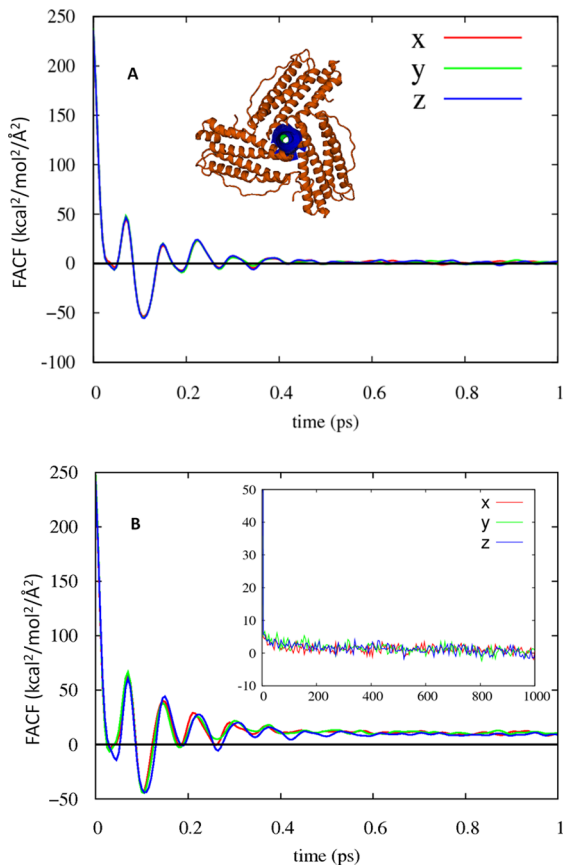


**Figure 1.** (A) FACF of  $\text{Fe}^{2+}$  in bulk water solution. Inset: arrangement of helices to form a 3-fold pore through the ferritin shell. (B) FACF of  $\text{Fe}^{2+}$  inside the ferritin channel ( $z = 13.5 \text{ \AA}$ ). Inset: long-time tail of this FACF. For both locations of the  $\text{Fe}^{2+}$  ion,  $x$ ,  $y$ , and  $z$  components of the FACF are presented.

atoms in total were run for 20 ns. The TIP3W model was used for water solvent molecules. The MD simulation systems were electrostatically neutralized, with Asp and Glu residues taken to be deprotonated (−1 charge) and His deprotonated (neutral). To set the temperature at 300 K, we used a Langevin thermostat. The thermostat damping coefficient was taken to be  $5 \text{ ps}^{-1}$ , and the time step was 1 fs per step. The external helices of each unit were fixed to prevent the dissociation of the three units during the simulations whereas the inner helices which form the channel were free to move. The interaction potential and size of  $\text{Fe}^{2+}$  were obtained from ref 45.

Extensive details of these MD simulations were presented in ref 50, where they were used to elucidate mechanistic details of the influx of iron through 3-fold pores in ferritin. Here we use the same simulations to provide input data for a coarse-grained model of ion permeation kinetics, namely 3D PNP theory. In particular, we use the MD simulations to generate the protein structural details needed to set up the PNP simulation system. This includes a set of atomic coordinates for the atoms in the 3-fold region of the protein, from which the geometric structure of the flow region through the channel was constructed. Visual inspection of the channel and binding sites was done using the visualization programs VMD<sup>56</sup> and PyMOL Molecular

Graphics.<sup>57</sup> The channel radius and center line were computed using the HOLE<sup>58</sup> program. Furthermore, to compute the internal diffusivity of  $\text{Fe}^{2+}$  ions as a function of their distance along the channel axis according to the force autocorrelation function procedure described in the next subsection, the net force on an  $\text{Fe}^{2+}$  ion fixed at a specified position along the channel axis was calculated every 5 fs.

**2.2. Force Autocorrelation Function (FACF) Method for Calculating Ion Diffusion Coefficients.** Calculation of the diffusion constant for an ion bulk water solution via all-atom MD simulation is straightforward. If  $r(t)$  is the distance the particle has moved at time  $t$  from its location at  $t = 0$ , then direct calculation of the ensemble average  $\langle r^2(t) \rangle$  for the ion gives a curve which is linear in time, and the slope of this curve can be read off to extract the diffusion constant  $D$  according to the Einstein relation  $\langle r^2(t) \rangle = 6Dt$ . Calculating an effective diffusion constant for a drift-diffusion process occurring in the interior of a narrow ion channel is more challenging. The ion is now subject to systematic forces (e.g., electrostatic forces due to interaction with charges on pore-lining amino acids). In analyzing the intrinsic diffusion coefficient relevant to the ion motion in a specified region of the channel, one must carefully subtract off the average systematic force on the ion. Temporal fluctuations in the force on the ion about this average value then serve as the random force function in a Langevin equation level description of the process.<sup>59,60</sup>

One appealing way to account for these effects is provided by the (random) force autocorrelation function (FACF) method. In this procedure, the ion is placed somewhere in space and held fixed (*in silico*) while all other atoms in the system (protein and water in this case) are allowed to evolve in an MD simulation brought to Boltzmann equilibrium. The time averaged force  $\langle \vec{F} \rangle$  on the ion is calculated. The temporal fluctuations about this average, i.e.,  $\vec{R}(t) = \vec{F}(t) - \langle \vec{F} \rangle$ , are identified as the random force on the ion. From this time series the random force autocorrelation function (FACF) can easily be constructed. Then, using the second fluctuation dissipation theorem<sup>61,62</sup> (and assuming Markovian friction), the friction constant associated with the ion is calculated as

$$\gamma = \frac{\int_0^\infty \langle R_z(t)R_z(0) \rangle dt}{k_B T} \quad (1)$$

where  $R_z(t)$  is the  $z$ -component of the random force vector. Finally, using the Stokes–Einstein relation,  $D = k_B T / \gamma$ . (We assume here that diffusion is isotropic, so that  $D_x = D_y = D_z = D$ . We have checked that this isotropy holds to a good approximation for  $\text{Fe}^{2+}$  inside ferritin, as illustrated in the Results.) We expect that the diffusion coefficient characterizing a particular ionic species will vary with the location of the ion inside the channel, reflecting the different molecular environment there. In particular, we expect  $D$  to decrease below its bulk solution value as the ion enters the channel, due to the geometric confinement supplied by the latter, as well as the imposition of large additional electrostatic forces on the ion by charged or partially charged chemical groups on the protein which are in close proximity to the aqueous pore. Indeed, our calculations on ions inside the ferritin channel show large effects of this type, leading to a significant reduction in ion diffusivity compared to bulk values (cf. section 3.1 below).

**2.3. Summary of Poisson–Nernst–Planck (PNP) Theory As Implemented via a 3D PNP Solver.** Ions are assumed to execute Brownian Dynamics in the overdamped

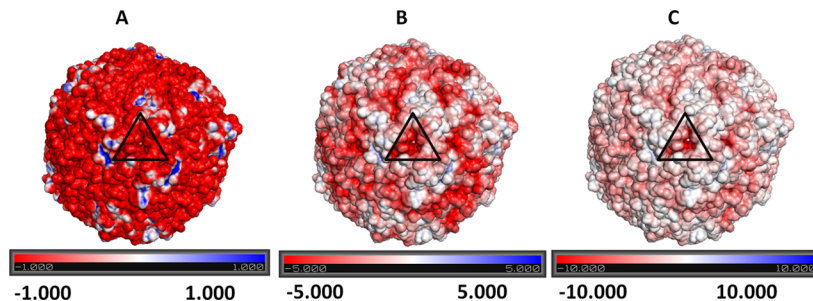


**Figure 2.** Electrostatic potential map for human H-chain ferritin, calculated by solving the Poisson equation (no mobile electrolyte ions) in APBS.<sup>65</sup> Negative potential is shown as red; positive potential, as blue. (The potential goes to zero far outside the ferritin molecule.) The black triangle highlights the location of one three-unit channel. Note the different potential scales in panels A, B, and C (units of potential are  $k_B T/e$ ).

limit, i.e., according to the Smoluchowski equation.<sup>63</sup> If the local concentration of the  $k$ th species of ions is  $c_k(\vec{r})$  and its local diffusion coefficient is  $D_k(\vec{r})$ , then the local flux of this ion species is given by

$$\vec{j}_k(\vec{r}) = D_k(\vec{r})[-\vec{\nabla}c_k(\vec{r}) + \beta\vec{F}_k(\vec{r})c_k(\vec{r})] \quad (2)$$

Here  $\beta = [k_B T]^{-1}$  and  $\vec{F}_k(\vec{r})$  is the local force acting on an ion of species  $k$ . Basic PNP is an electro-diffusion model; i.e., the relevant force is taken to be the electrostatic force provided by all other charges in the system.<sup>64</sup> This force depends on the local electric field, or equivalently, on the electrostatic potential profile  $\phi(\vec{r})$ . Specifically:  $\vec{F}_k(\vec{r}) = -q_k\vec{\nabla}\phi(\vec{r})$ , where  $q_k$  is the charge of an ion of species  $k$ . (Note: In addition to this electrostatic force, there is a strong repulsive force that prevents ions from moving through the “walls” of the channel or the membrane. These excluded volume interactions can be incorporated into boundary conditions for the Nernst–Planck Equations introduced below.) In general,  $c_k(\vec{r})$  and  $\phi(\vec{r})$  evolve in time. Here we will concern ourselves only with steady state ion flow, so that ion concentration and electric potential profiles are time-independent. For steady state concentrations to obtain, we must have  $\vec{\nabla}\cdot\vec{j}_k(\vec{r}) = 0$ . Thus, the following drift-diffusion equation, designated as the Nernst–Planck (NP) equation, must be satisfied for each of the  $K$  ionic species in the system:

$$0 = \vec{\nabla}\cdot\{D_k(\vec{r})[\vec{\nabla}c_k(\vec{r}) - \beta\vec{F}_k(\vec{r})c_k(\vec{r})]\} \\ k = 1, 2, \dots, K \quad (3)$$

The electric potential depends on the location of fixed charges in the system as well as the mobile ion charge distributions. Charges fixed on the protein arise due to deprotonation of acidic residues or protonation of basic residues; electronic polarization of neutral moieties within the protein can also lead to effective partial charges on certain atoms. Although the electrolyte solution must be overall charge neutral, the positive and negative ions in general adjust differently to the electric fields within the system, leading to local imbalance of mobile charge at a given point in space. Adopting a mean-field approximation based on the presumed steady state mobile ion distributions, we solve the Poisson equation to determine  $\phi(\vec{r})$ :

$$\vec{\nabla}\cdot(\epsilon(\vec{r})\vec{\nabla}\phi(\vec{r})) = -4\pi[\rho_{\text{fixed}}(\vec{r}) + \sum_{k=1}^K q_k c_k(\vec{r})] \quad (4)$$

where  $\epsilon(\vec{r})$  is the static dielectric coefficient profile and  $\rho_{\text{fixed}}(\vec{r})$  is the local density of fixed charge. We discretize the NP

equations (one for each ion species), i.e., eq 3, and also the Poisson equation (4) onto 3D rectangular grids. Supplemented by appropriate boundary conditions, these equations can then be updated self-consistently to convergence. The relevant boundary conditions for the NP equations are, for each ion species, the prescribed ion concentrations in the reservoir on either side of the channel/membrane system (or ferritin shell, in the case of direct interest here) and zero flux boundary conditions at the boundaries between the aqueous flow system and the protein pore and membrane (or ferritin shell). For the Poisson equation (4), if there are no externally applied electric fields we set  $\phi = 0$  on the boundaries of the electrostatic simulation box. While this is clearly the appropriate boundary condition for a standard membrane spanning ion channel, the situation could in principle be different for the 3-fold pores in ferritin because the internal cavity reservoir is not infinite in size and there are other charged species (especially, the other 3-fold channels in the ferritin shell) in close proximity to the pore selected for PNP analysis. To ascertain whether there is any significant intrinsic difference between the electric potential in the central cavity vs that infinitely far from the protein in the cytoplasm, we inserted the entire 24-subunit ferritin molecule into the APBS Poisson–Boltzmann equation solver.<sup>65</sup> Following a similar analysis on ferritin-like molecules by Ceci et al.,<sup>43</sup> we set the salt concentration to 0 for this calculation, i.e., solved the Poisson equation. We found an intrinsic potential difference of only  $\sim 0.1 k_B T/e$ , which justifies the  $\phi = 0$  boundary condition noted above. Figure 2 shows the electrostatic potential of the entire ferritin molecule. The following features merit emphasis: (i) Charges distributed throughout the ferritin molecule generate a weak negative potential at its cytoplasmic edge. (ii) Only the 3-fold channels are strongly (negatively) charged. Moreover, the 3-fold channels are far enough apart that each 3-fold channel can be considered in isolation from the rest of the ferritin molecule as far as electrostatic forces are concerned. This provides justification for the PNP model developed, which includes only one 3-fold channel (neglecting any electric fields generated by other charged atoms in the protein).

Once converged ionic concentration profiles and the electric potential profile have been obtained after numerical solution of the PNP equations, we appeal to eq 2 for the steady state ion fluxes to extract the ion current of each species moving through the aqueous channel.

### 3. RESULTS

#### 3.1. FACP Calculation of the $\text{Fe}^{2+}$ Ion Diffusivity Profile.

Of primary interest here is the spatial diffusivity profile

of  $\text{Fe}^{2+}$ . In Figure 1A we show  $\langle R_\alpha(t) R_\alpha(0) \rangle$ ,  $\alpha = x, y, z$ , for an  $\text{Fe}^{2+}$  ion in bulk water and in Figure 1B for an ion at the position  $z = 13 \text{ \AA}$  inside the channel. (See Figure 3 for the

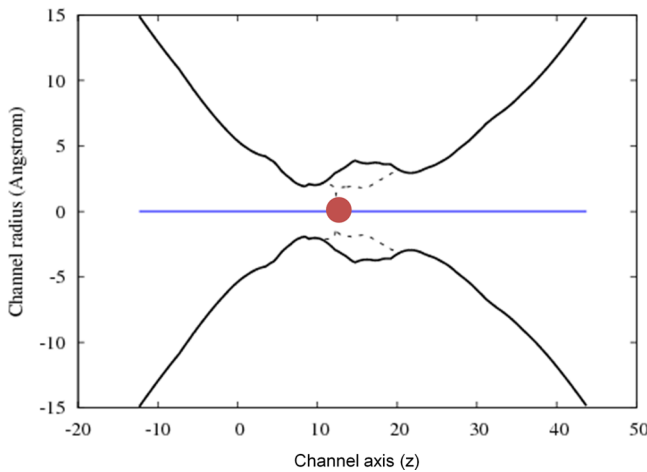


**Figure 3.** Black solid line: channel radius obtained from the HOLE program<sup>58</sup> when an ion is not inside the channel. Black dotted line: channel radius when a  $\text{Na}^+$  ion (red circle) is inside the channel.

orientation of the ferritin pore with respect to the  $z$  axis.) Importantly, we find that the correlation functions for  $x, y, z$  components of the  $\text{Fe}^{2+}$  ion diffusivity coefficient at a given value of channel axis coordinate  $z$  are very similar, thus giving credence to our assumption in the PNP analysis outlined above that ion diffusivity, though spatially dependent, is isotropic everywhere. For an ion bulk water the FACF exhibits damped oscillation, and quickly decays to zero (in less than 1 ps; cf. Figure 1A). In the case where the  $\text{Fe}^{2+}$  ion is located well inside the channel, after an initial period of oscillation and partial decay, the correlation function reaches a regime where it decays monotonically but very slowly to 0. The full decay of this correlation function tail can take as long as 1000 ps (cf. Figure 1B). This slow temporal decay gives rise to a large time integral of the FACF and hence a large local friction constant (or, equivalently, a small local diffusion coefficient).

Using the procedure described above, we obtained a value of  $7 \times 10^{-6} \text{ cm}^2/\text{s}$  for the bulk diffusion constant of  $\text{Fe}^{2+}$  in water at room temperature and 1 atm pressure. This compares well with the experimentally measured value of  $7 \times 10^{-6} \text{ cm}^2/\text{s}$ .<sup>49</sup> Figure 4 shows the spatial diffusivity profile of an  $\text{Fe}^{2+}$  ion along the channel axis, extracted using the FACF method. Clearly, the local diffusion coefficient varies significantly with the ion's position along the channel axis. (Because of this feature, we will reserve the term "diffusion constant" for the value of  $D$  in bulk solution or its average value inside the channel. Otherwise, we will refer to this quantity as the spatially dependent diffusion coefficient or diffusivity profile.) Note the large reduction of  $D$  for an ion residing inside the pore relative to its bulk solution value. The reduction factor depends on the location of the ion within the channel, with a maximum reduction factor of ca. 900 times and an average reduction factor (based on the rough channel length indicated in the figure) of ca. 400 times smaller.

To explore and calibrate the large reduction in the internal diffusion coefficient for  $\text{Fe}^{2+}$ , we performed similar calibrations for two monovalent ions,  $\text{Na}^+$  and  $\text{K}^+$ . Previous calculations of the internal diffusion coefficient for narrow ion channels<sup>66,67</sup> have found a reduction of less than a factor of 15 for

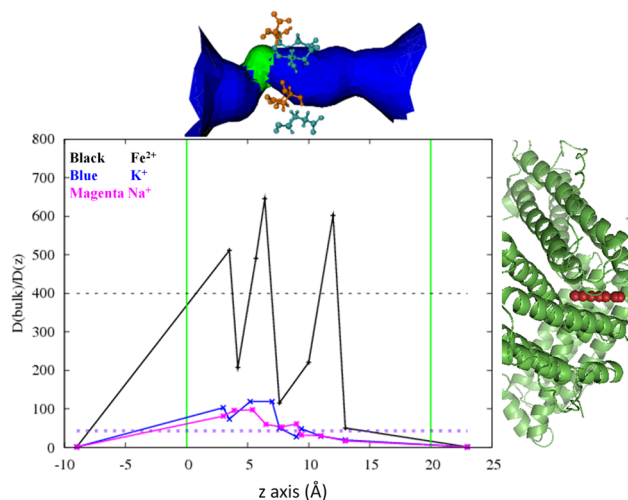


**Figure 4.** Top: ion channel surface obtained from the Hole program. The blue color denotes a region where the pore radius is  $>2.30 \text{ \AA}$ , and the green color denotes a region where  $1.15 \text{ \AA} < \text{pore radius} < 2.30 \text{ \AA}$ . Glu (cyan) and Asp (orange) residues are indicated. Right: 3-fold channel and the positions of  $\text{Fe}^{2+}$  or other positive ions (shown as red balls) inside the channel used in FACF calculations. Left: diffusion coefficient along the channel obtained using the FACF method. (The bulk diffusion constant calculated via the FACF method is  $7 \times 10^{-6} \text{ cm}^2/\text{s}$ .) Key: black,  $\text{Fe}^{2+}$ ; magenta,  $\text{Na}^+$ ; blue,  $\text{K}^+$ ; vertical green line at  $z = 20 \text{ \AA}$ , cytoplasmic entrance; vertical green line at  $z = 0 \text{ \AA}$ , exit to inner cavity. The average over all data points of the internal  $\text{Fe}^{2+}$  diffusion coefficient (i.e., the data points at values of  $z$  between the two vertical green lines) is ca. 400 times smaller (dashed black horizontal line) than the bulk diffusion constant. The corresponding average for the internal  $\text{Na}^+$  and  $\text{K}^+$  diffusion coefficients is ca. 40 times smaller (dashed magenta horizontal line for  $\text{Na}^+$ ; dashed blue horizontal line for  $\text{K}^+$ ) than the corresponding bulk diffusion constant.

monovalent ions inside a narrow channel (sufficiently narrow to require single file ion motion through the pore). Here we first computed the diffusion constant for  $\text{Na}^+$  and  $\text{K}^+$  in bulk water using the FACF method described above. We obtained values of  $11 \times 10^{-6}$  and  $15.5 \times 10^{-6} \text{ cm}^2/\text{s}$  for  $\text{Na}^+$  and  $\text{K}^+$ , respectively, which are in good agreement with experiment ( $13.3 \times 10^{-6}$  and  $19.6 \times 10^{-6} \text{ cm}^2/\text{s}$  for  $\text{Na}^+$  and  $\text{K}^+$ , respectively<sup>68,69</sup>). Then we computed the internal  $D(z)$  diffusivity profile for a  $\text{Na}^+$  ion along the channel axis. The results are shown in Figure 4. The reduction in diffusion coefficient relative to the bulk value is not as large as for  $\text{Fe}^{2+}$ , but it is still striking: there is a maximum reduction factor of 65 and an average reduction of ca. 40. Our goal in studying the diffusivity profile of monovalent ions in this work is to calibrate against the corresponding  $\text{Fe}^{2+}$  results, and against previous results for monovalent ions inside ion channels. The fact that we obtain essentially the same results for  $\text{Na}^+$  and  $\text{K}^+$  provides a consistency check on our calculations in ferritin.

What is the source of the large increase in internal friction calculated for both  $\text{Fe}^{2+}$  and  $\text{Na}^+$ ? The six negatively charged side chains along the narrow channel form two rings ca. 5  $\text{\AA}$  apart, which provide electrostatic binding sites that stabilize cations in the pore. Such binding sites have in fact been observed in several previous crystallographic studies of ferritin.<sup>70,71</sup> Furthermore, the channel forms a kink at its point of narrowest construction (cf. Figure 5) that further hinders the escape of the permeant ions.

**3.2. Construction of the PNP Simulation System.** X-ray structures of the ferritin protein indicate that there are multiple

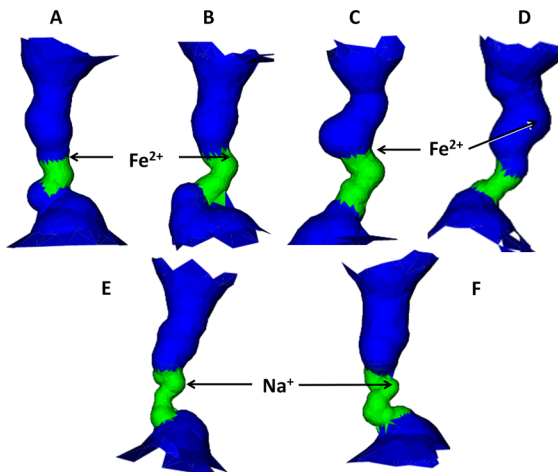


**Figure 5.** HOLE program rendering of 3-fold pore channel snapshots taken from several different MD simulation runs with an  $\text{Fe}^{2+}$  ion (A)–(D) or an  $\text{Na}^+$  ion (E), (F) fixed at various positions inside the channel as indicated. Key: blue, pore radius  $> 2.30 \text{ \AA}$ ; green,  $1.15 \text{ \AA} < \text{pore radius} < 2.30 \text{ \AA}$ . Note that some amount of kinking is always present.

pores connecting the external (cytoplasmic) region and the inner core (inside the ferritin protein shell). Most are formed at the boundaries of subunits of the proteins and can be classified by the symmetry of these boundaries, namely: 2-fold, 3-fold, and 4-fold symmetric sites. There are also direct conduits through a single subunit, designated as 1-fold pores. Experiments have shown that the 3-fold pores provide the primary conduction pathway for  $\text{Fe}^{2+}$  ions entering the ferritin interior from the cytoplasm.<sup>35,71–73</sup> Indeed, our own prior MD simulations support this hypothesis.<sup>50</sup> Hence we will focus here on calculating the rate of  $\text{Fe}^{2+}$  influx through a typical 3-fold channel, using 3D PNP theory as implemented via the finite-difference solver described above.

A snapshot of the 3-fold pore taken from our MD simulations is shown in Figure 6. 3D PNP theory was developed for computing ion currents through an ion channel protein embedded in a lipid bilayer membrane. Ferritin is not a standard ion channel in this regard. There is no lipid bilayer. Instead, the remainder of the protein shell serves as an effective membrane in that it prevents  $\text{Fe}^{2+}$  ions from flowing freely into the ferritin interior—the ions must traverse the narrow 3-fold pores in the shell. To utilize our 3D PNP solver to compute  $\text{Fe}^{2+}$  flux into ferritin, we construct a simulation system as depicted in Figure 7. The pore region is based directly on a

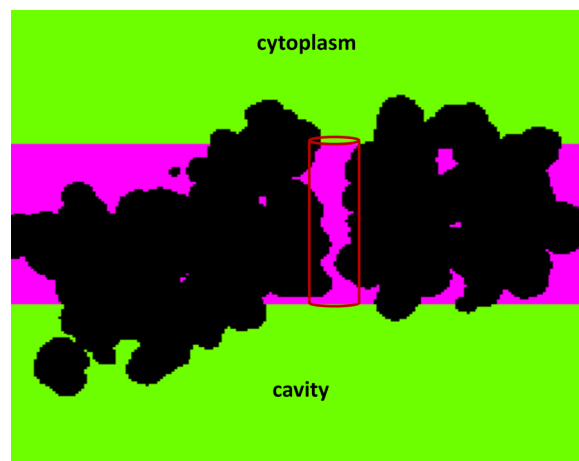


**Figure 7.** Initial ferritin conformation selected for PNP calculations. Black: 3-unit channel. Green: cytoplasmic and inner cavity bathing solutions. The magenta slab region is analogous to the bilayer membrane in a standard ion channel. The red cylinder is generated by the PNP solver algorithm to place the membrane slab relative to the protein pore. The ion flow region extends from the cytoplasmic bath through the magenta region contained within the red cylinder inside the pore. (Ions reaching the cap of the red cylinder that abuts the cavity reservoir are subjected to an absorbing boundary condition for the calculation of  $\text{Fe}^{2+}$  influx currents.)

snapshot from our MD simulation, which is rendered onto a spatial simulation grid just as we would with a standard transmembrane ion channel.<sup>64,74–77</sup> We then impose an artificial membrane, i.e., a low dielectric slab outside of the pore structure which is impermeable to ions. (In previous studies of standard ion channel systems<sup>64,74,75,78</sup> we have found that precise details of the bilayer membrane outside the channel pore do not critically affect ion flow through the channel beyond the properties just noted, namely blockage of ion flow through the channel and low dielectric constant.) We assign a width of  $20 \text{ \AA}$  to the dielectric slab representing the artificial bilayer, consistent with the width of the ferritin protein shell. The dielectric constant of this slab is assigned the value  $\epsilon = 20$ . The protein region is taken to have the same value ( $\epsilon = 20$ ), while the aqueous regions of the system (both inside and outside the channel) are assigned the value  $\epsilon = 80$ . For initial conditions, we set a nonzero value of bulk  $\text{Fe}^{2+}$  concentration in the cytoplasmic reservoir. (This is balanced, electrostatically, by including twice this concentration of  $\text{Cl}^-$  ions in the cytoplasmic reservoir. However, no anions permeate into the

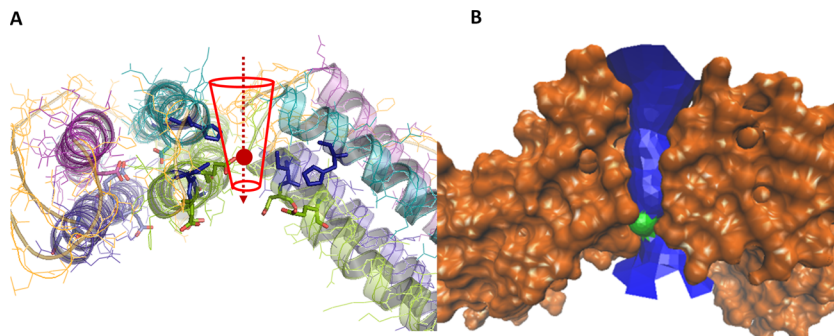


**Figure 6.** (A) and (B) 3-fold channel via two different representations. Panel A shows the pathway of ions (red arrow). Panel B shows the shape of the pore (ion flow space). In panel B, blue indicates pore radius  $> 2.30 \text{ \AA}$  and green denotes  $1.15 \text{ \AA} < \text{pore radius} < 2.30 \text{ \AA}$ .

channel due to the very large electrostatic energy barrier generated by the 3 Glu and 3 Asp residues that line it.) An  $\text{Fe}^{2+}$  ion that reaches the internal edge of the ferritin shell after traversing the 3-fold pore quickly diverts to one of the ferroxidase centers, where it combines with hydrogen peroxide or  $\text{O}_2$  to eventually form inert  $\text{Fe}_2\text{O}_3$ . The latter is incorporated as a mineral at the center of the ferritin interior core. Here we represent this sequence of events by placing an absorbing boundary condition at the internal entrance to the 3-fold ferritin pore. Within the drift-diffusion model that underlies PNP theory, this is accomplished by setting the concentration of  $[\text{Fe}^{2+}]$  (and  $[\text{Cl}^-]$ ) to 0 in the interior reservoir.

For completeness, we have also calculated  $\text{Fe}^{2+}$  flux for the reverse process, i.e.,  $\text{Fe}^{2+}$  ions inside the ferritin interior core and none (or a negligibly small number) outside. This situation presumably occurs when  $\text{Fe}^{3+}$  in the mineral core is converted back to  $\text{Fe}^{2+}$  to reinject it into the cytoplasm. Interestingly, we find similar  $\text{Fe}^{2+}$  ion currents under similar driving conditions for the  $\text{Fe}^{2+}$  influx and efflux processes, as described in detail below.

Given the PNP simulation system outlined above, the lattice-discretized PNP partial differential equations are iterated to self-consistency. As output we obtain 3-D grid representations of the electric potential and the concentration profiles of both ionic species ( $\text{Fe}^{2+}$  and  $\text{Cl}^-$ ) everywhere in space. A 2D slice of the 3D electric potential and the associated cation and anion concentrations obtained from a typical PNP calculation are shown in Figure 8. One sees immediately that  $\text{Cl}^-$  ions do not permeate into the interior of the ferritin shell, for reasons discussed above. We also present 1-D plots of the electric potential and  $\text{Fe}^{2+}$  density profiles along the channel axes in Figures 9 and 10, respectively.

As noted above, the PNP equations directly specify the current density of each ion species everywhere in space in terms of the electric potential and ionic concentration profiles at steady state (eq 2). These current densities can be integrated over an appropriate surface (e.g., a transverse patch of surface area within the channel pore) to obtain the net flux of ions through the pore, and hence the net electric current.

The physiological concentration of  $[\text{Fe}^{2+}]$  in the cytoplasm is very low, ca.  $10^{-5}$  M. (The precise value depends on cytoplasmic conditions and may vary over several orders of magnitude.<sup>49,79</sup>) This renders infeasible direct simulation of the kinetics of  $\text{Fe}^{2+}$  influx by all-atom nonequilibrium molecular dynamics (NEMD)<sup>80,81</sup> or even by coarse-grained Brownian dynamics:<sup>76,82,83</sup> the number of ion permeation events would be far too low to extract an ion current with statistical reliability. PNP is more flexible in this regard, because it does not track real-time molecular trajectories. Rather it solves coupled nonlinear partial differential equations, with their solution (electric potential and mobile ion concentration distributions) representing the desired steady state, including predictions for ion currents through the system as described above. However, the nonlinear PNP equations become difficult to converge numerically at very low ionic concentration. In practice, with our PNP solver we are limited to  $\sim 0.005$  M  $\text{FeCl}_2$  concentration in the cytoplasmic bath. We thus must invoke some type of extrapolation scheme to extend from the low concentrations that we can access with our PNP solver to the very low physiological concentration of  $[\text{Fe}^{2+}]$  in the cytoplasm. In the present study, we fit data points on a current-concentration ( $I$ - $C$ ) curve to a Michaelis-Menten (MM) functional form, i.e.:

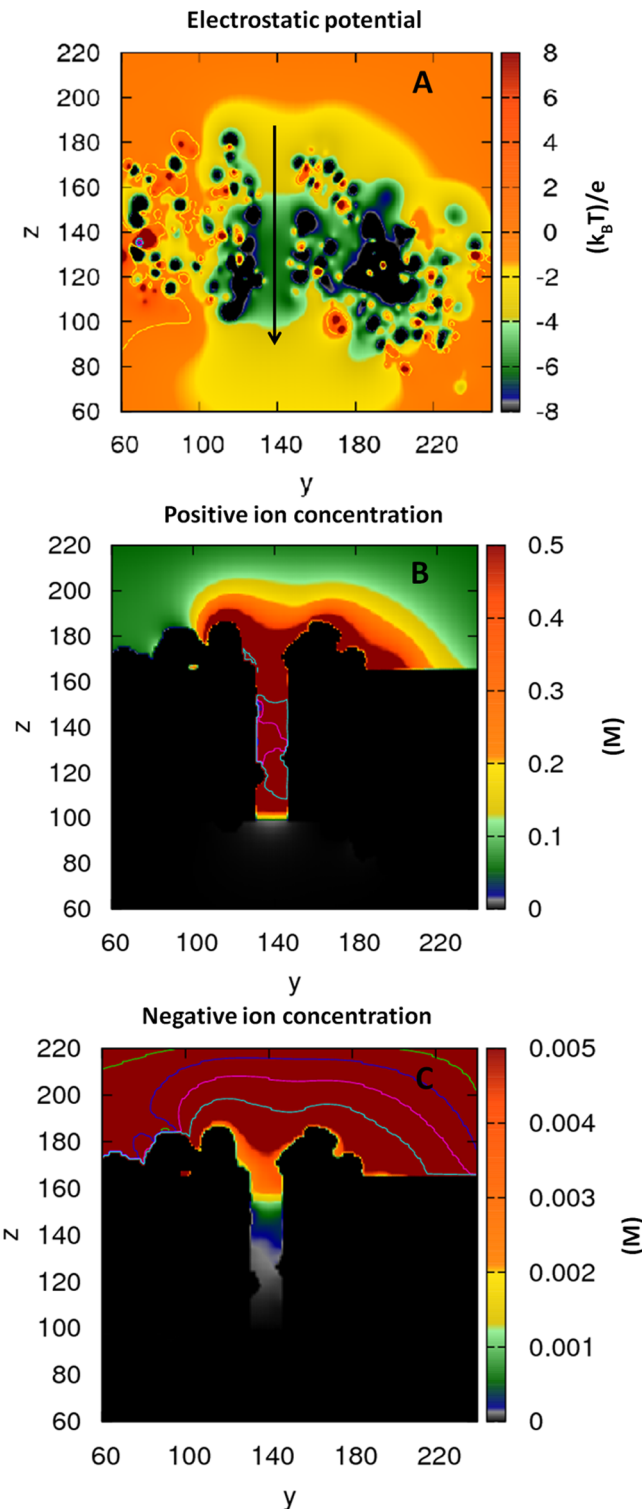


**Figure 8.** Two-dimensional slice of the (three-dimensional) electrostatic potential (panel A) and mobile ion concentration of cations (panel B) and anions (panel C) for the 3-fold channel calculated via PNP.  $y$  and  $z$  axes show the grid points used in the PNP calculation (grid point spacing =  $1/3$  Å); the channel spans from grid points 100 to 160 along the  $z$  axis.

$$I = \frac{I_{\max}[\text{Fe}^{2+}]}{C_{\max} + [\text{Fe}^{2+}]} \quad (5)$$

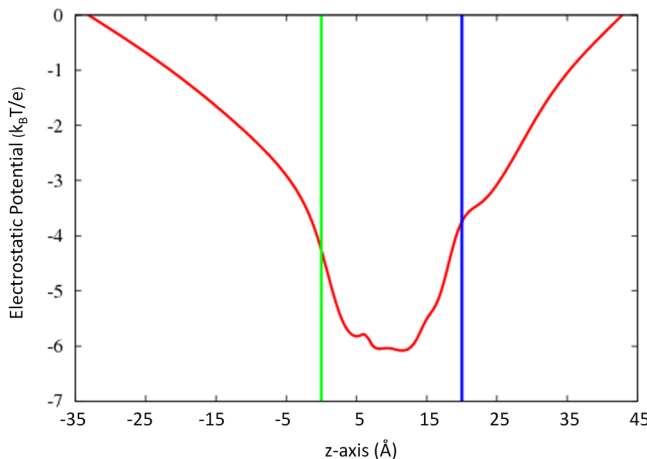


**Figure 9.** Electrostatic potential along the channel ( $z$ ) axis. Blue vertical line: cytoplasmic entrance of the channel; green vertical line: exit to the inner cavity region.

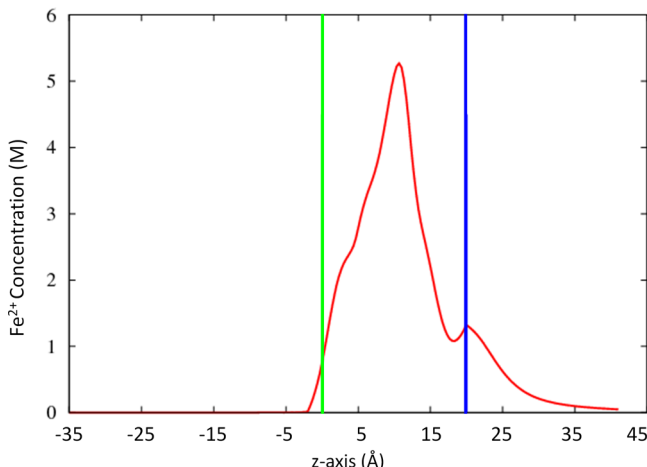


**Figure 10.** Red:  $\text{Fe}^{2+}$  concentration along the channel ( $z$ ) axis. Blue vertical line: cytoplasmic entrance of the channel; green vertical line: exit to the aqueous cavity inside the ferritin protein coat. The bulk cytoplasmic concentration of  $\text{Fe}^{2+}$  is 0.05 M.

We have found in previous work on other ion channels that this functional form provides an accurate description of the saturation behavior of  $I-C$  curves with increasing ionic strength of the nonzero bathing solution that drives ionic flux through the channel.<sup>84,85</sup> In the present study, we adjust the parameters  $I_{\max}$  and  $C_{\max}$  to optimize the fit to our computed  $I-C$  data points, and then extrapolate eq 5 down to the physiologically relevant concentration of ca.  $10^{-5}$  M  $\text{Fe}^{2+}$ .

Figure 11 shows a typical set of data points under conditions of 0 M  $[\text{Fe}^{2+}]$  inside the ferritin channel when the electric potential difference inside vs outside the ferritin cavity is set to zero. (Note: For computational simplicity, in these PNP calculations we approximated the spatially varying internal spatial diffusivity profile with its average, i.e., a single internal diffusion constant 1/400 times that of the bulk  $\text{Fe}^{2+}$  diffusion constant, as explained in Figure 4.) The optimized MM fit to these data points is also indicated. Using the MM fit, we estimate an inward  $\text{Fe}^{2+}$  ionic flux at  $2 \times 10^{-5}$  M  $[\text{Fe}^{2+}]$  in the cytoplasmic reservoir of 184.4  $\text{Fe}^{2+}$  ions/s. By inverting this flux, we can estimate the transit time of a single  $\text{Fe}^{2+}$  ion inward through the 3-fold pore of ferritin as ca. 5.4 ms. This number is

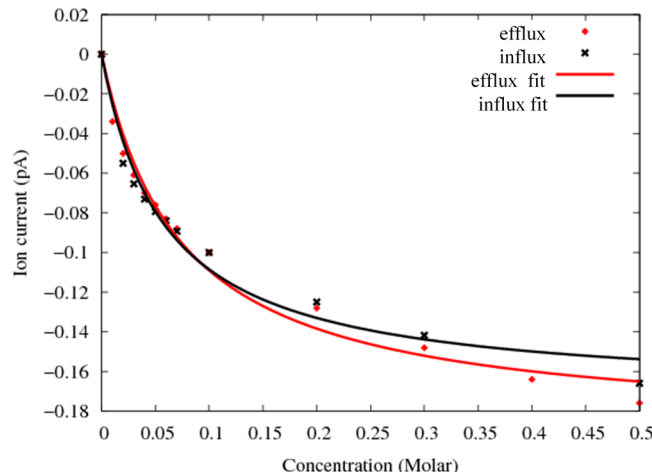


**Figure 11.** Current–concentration ( $I-C$ ) curves are shown for influx ( $[\text{Fe}^{2+}] = 0$  in the ferritin cavity) and efflux ( $[\text{Fe}^{2+}] = 0$  in the cytoplasm) permeation processes. In both cases the electric potential difference between the two aqueous reservoirs is set to 0.

in good agreement with the estimation of the same transit time given by Chasteen and co-workers,<sup>49</sup> who conducted their experiments at cytoplasmic  $[\text{Fe}^{2+}]$  close to  $2 \times 10^{-5}$  M. [Note that, according to Figure 11,  $10^{-5}$  M lies well in the linear (low  $[\text{Fe}^{2+}]$ ) regime of the  $I-C$  curve, so inward  $\text{Fe}^{2+}$  flux should scale linearly with cytoplasmic  $\text{Fe}^{2+}$  concentration under physiological conditions.]

Efflux of iron from the ferritin core is instigated by dissolution of the mineral core, whereby  $\text{Fe}^{3+}$  is converted to  $\text{Fe}^{2+}$  in significant quantities. The release of  $\text{Fe}^{2+}$  can be detected experimentally under physiological conditions.<sup>86</sup> (Although the exact trigger for this process is not well understood *in vivo*, spectroscopic studies *in vitro* have shown that a number of chemical agents including urea and biologically relevant riboflavin derivatives trigger efflux of  $\text{Fe}^{2+}$  from the core. The initial reductive step results in an internal  $[\text{Fe}^{2+}]$  much higher than  $[\text{Fe}^{2+}]$  in the cytoplasm.<sup>87</sup> This  $\text{Fe}^{2+}$  can then exit the 3-fold pores via a Fick's Law driving force. To probe the details of the  $\text{Fe}^{2+}$  efflux process, we repeated the computation described above with a nonzero fixed  $[\text{Fe}^{2+}]$  value inside the ferritin shell and  $[\text{Fe}^{2+}] = 0$  in the cytoplasm. The resultant  $I-C$  curve is also shown in Figure 11. Interestingly, it closely resembles the  $I-C$  curve computed for the influx process, which would imply a similar time scale for  $\text{Fe}^{2+}$  efflux as for influx of ions at similar driving concentrations of  $\text{Fe}^{2+}$ .

#### 4. DISCUSSION AND CONCLUSIONS

In a standard membrane spanning ion channel protein, the transit time of an individual ion is typically on the order of 10–100 ns. For ferritin, experimental estimation of the time for an  $\text{Fe}^{2+}$  to pass from the cytoplasmic entrance to the exit of the protein coat into the internal aqueous region is on the millisecond time scale. What factors could account for the much slower ion transit through ferritin? One possibility is that the electrostatic binding sites inside the 3-fold ferritin pore are so strong that ions entering the pore become stuck for a long time in deep attractive potential wells. Our recent MD simulations of  $\text{Fe}^{2+}$  flow through 3-fold pores in ferritin did not show such an effect.<sup>50</sup> No evidence for infrequent barrier crossing events was seen. In contrast, using a very large (~20 M) cytoplasmic  $\text{Fe}^{2+}$  concentration in our MD simulations, we

found that  $\text{Fe}^{2+}$  traversed the channel rather quickly – in a few nanoseconds. Of course the physiological concentration of cytoplasmic  $\text{Fe}^{2+}$  is very low, ca.  $10^{-5}$  M, which goes a long way toward explaining the slow transit through the channel. In contrast, typical physiological concentrations of ions like  $[\text{Na}^+]$  and  $[\text{Cl}^-]$  are in the  $\sim 0.1$  M range, consistent with larger Fick's law driving forces than in the case of  $\text{Fe}^{2+}$  into ferritin, and hence larger ion fluxes and smaller ion transit times. With our 3D PNP solver, we can simulate steady state conditions of nonequilibrium ion flux down to ca. 0.005 M cytoplasmic  $\text{Fe}^{2+}$ . By extrapolation of the  $I$ – $C$  curve down to  $10^{-5}$  M, we are able to estimate the inward flux through the 3-fold ferritin pores. The ion currents obtained in this manner are indeed much lower than typical currents observed in standard ion channels. Inverting the ion current, we can obtain a crude estimate of the transit time per  $\text{Fe}^{2+}$  ion. Our computational study has determined this transit time through the 3-fold channels to be in the millisecond time scale regime, consistent with experimental estimates.

Apart from the low concentration of  $\text{Fe}^{2+}$ , there is another factor that strongly influences the long time scales found for  $\text{Fe}^{2+}$  influx into ferritin in our PNP calculations, namely, the low values of the diffusion coefficients that govern motion of ions inside the 3-fold ferritin channels. The FACF analysis performed in this work indicates an extremely large reduction relative to the bulk water diffusion constant of  $\text{Fe}^{2+}$  when the ion penetrates deep into the 3-fold ferritin channel. We estimated an average reduction factor of the intrapore diffusion coefficient of ca. 400. Since the flux of ions according to the NP equation scales with the diffusivity profile in the flow space (inside the channel), this reduction factor will translate into a similar reduction factor for the ion current, with a concomitant increase in the ion transit time. In standard membrane-spanning ion channels that pass monovalent ions, a reduction in the internal diffusion coefficient relative to the bulk diffusion constant by a factor of ca. 10 times is expected for narrow (single file passage) channels, with a less severe reduction occurring in wider channels. Again, this helps to explain the extremely large reduction in ion current obtained for  $\text{Fe}^{2+}$  influx into ferritin relative to typical ion currents in standard ion channels. We traced the large reduction in ion diffusivity within the channel to two unique features of the ferritin 3-fold pores, namely, (i) the existence of two negative rings of charge (from a trio of deprotonated glutamates and a trio of deprotonated aspartates) separated by  $<5$  Å along the channel pore, and (ii) a kinking of the pore that occurs in the same region of the channel. We would intuitively expect both features to inhibit ion diffusion through the pore. We would also expect these effects to be enhanced for a divalent ion like  $\text{Fe}^{2+}$  relative to the behavior of a monovalent ion like  $\text{Na}^+$ , due to stronger coulomb forces experienced by the divalent ion. These forces will affect both the average force felt on a permeant ion and the magnitude of the temporal fluctuations about the average, thus increasing the size of the random force autocorrelation function and ultimately of the local friction constant.

Although we were primarily concerned here with the influx of  $\text{Fe}^{2+}$  into the 3-fold ferritin pore, we also considered the reverse process, i.e., the situation where there is a significant excess of  $\text{Fe}^{2+}$  in the aqueous cavity that lies inside the protein shell relative to the amount in the cytoplasmic exterior (which is indeed tiny). Such a concentration gradient generates a Fick's Law driving force for expulsion of  $\text{Fe}^{2+}$  to the cytoplasm through 3-fold pores. The efflux process is less well understood,

particularly *in vivo*, as to how and what agents trigger the reduction of  $\text{Fe}^{2+}$ , how electron transfer to the mineral core occurs, etc. However, several experimental studies suggest that  $\text{Fe}^{2+}$  ions exit to the cytoplasm via the 3-fold pores once the reduction has taken place. (This process may be further regulated by a gating process in which the N terminal part of the bundle acts as a gate that opens or closes to control  $\text{Fe}^{2+}$  passage through the pore.)<sup>88</sup> Interestingly, we found that the current–voltage ( $I$ – $V$ ) curve for this putative efflux process was quite similar to the corresponding influx curve. This is perhaps surprising given the geometric asymmetry of the 3-fold pore with respect to reflection through a transverse central plane. It may point to the importance of the double ring of negative charges inside the channel described above. Their tendency to attract positive ions into the channel, but not to bind them so strongly that they get permanently stuck inside it, works in a similar fashion for cations entering from either the cytoplasm or the internal mineral cavity (cf. Figure 9).

The procedure we have used to estimate ion fluxes and transit times of  $\text{Fe}^{2+}$  flow through the 3-fold pores of ferritin is not without its flaws. PNP theory is far from exact. It is a mean-field theory, essentially a nonequilibrium version of Poisson–Boltzmann (PB) theory. Correlation effects that are neglected in the mean-field approximation are known in the context of equilibrium PB theory to be significantly more prominent for divalent ions than for multivalent ones.<sup>89,90</sup> Presumably, a similar situation holds in the nonequilibrium PNP case. Furthermore, in a PNP calculation we compute ion flux through the channel. We have assumed here that the inverse of the ion flux (number of ions passing through the channel per second) gives the time it takes for one ion to pass from entrance to exit of the channel. One can imagine kinetic scenarios where this relation fails. However, if there is a steady flow of ions through the channel and there are not too many binding sites (in ferritin there are 3 binding sites seen in X-ray structures and in MD simulations), the inverse of the current should serve as a rough but reasonable measure of the time scale for a typical ion to move through the channel.

In addition, the primitive form of PNP theory employed here gives only a coarse measure of the molecular level driving forces ("drift forces") that a permeant ion experiences in traversing the channel. We've assumed a simple electrostatic model of these forces. A more accurate measure of the force field experienced by an ion in the channel could be obtained by calculating the single-ion potential of mean force (PMF) from an all-atom simulation. Indeed, this would be a useful next step in studying ion permeation through ferritin. The version of PNP theory employed here also assumes a rigid pore structure that forms a conduit through which mobile ions can move. In fact, our MD simulation indicates that the protein pore (here the 3-fold pore region of ferritin) fluctuates considerably (see, for example, Figures 3 and 5 of the present study). Some of these fluctuation effects can be folded into a single-ion PMF calculation, which averages explicitly over protein fluctuations, with the net PMF function inputted as the single-particle potential in an otherwise standard PNP calculation.<sup>75</sup>

Despite its relative simplicity, our computational approach has proven successful in reproducing experimentally relevant properties such as the millisecond time scale for  $\text{Fe}^{2+}$  ion influx from the cytoplasm into the inner cavity. It has also provided insights into the slowness of this influx process compared to analogous processes in standard membrane-spanning ion protein channel proteins whose permeation pathways bear

some structural similarity (e.g., in pore radius, length of the channel, charged amino acid rings that guide select ions into the pore, etc.). Unlike experiments, this approach has enabled us to study the kinetics of iron uptake into ferritin by looking at both the diffusional components and the interactions of the  $\text{Fe}^{2+}$  ions with the electrostatic gradients inside the channel. Future work will concentrate on improved estimation of drift forces, ion residence times, passage of ions other than  $\text{Fe}^{2+}$ , and other aspects which should provide novel mechanistic details on the atomistic scale to elucidate how ferritin functions *in vivo*.

## AUTHOR INFORMATION

### Corresponding Author

\*R. D. Coalson: phone, (412) 624-8261; fax, (412) 624-8611; e-mail, coalson@pitt.edu.

### Notes

The authors declare no competing financial interest.

## ACKNOWLEDGMENTS

This work was supported in part by NSF Grant CHE-0750332 and through TeraGrid resources provided by the Pittsburgh Supercomputing Center, NICS, PSC, and TACC.

## REFERENCES

- (1) Andrews, S. C. The Ferritin-Like Superfamily: Evolution of the Biological Iron Storeman from a Rubrerythrin-Like Ancestor. *Biochim. Biophys. Acta, Gen. Subj.* **2010**, *1800*, 691–705.
- (2) Ebrahimi, K. H.; Bill, E.; Hagedoorn, P.-L.; Hagen, W. R. The Catalytic Center of Ferritin Regulates Iron Storage Via  $\text{Fe}(\text{II})\text{-Fe}(\text{III})$  Displacement. *Nat. Chem. Biol.* **2012**, *8*, 941–948.
- (3) Bou-Abdallah, F. The Iron Redox and Hydrolysis Chemistry of the Ferritins. *Biochim. Biophys. Acta, Gen. Subj.* **2010**, *1800*, 719–731.
- (4) Bou-Abdallah, F.; Santambrogio, P.; Levi, S.; Arosio, P.; Chasteen, N. D. Unique Iron Binding and Oxidation Properties of Human Mitochondrial Ferritin: A Comparative Analysis with Human H-Chain Ferritin. *J. Mol. Biol.* **2005**, *347*, 543–554.
- (5) Theil, E. C. Ferritin Protein Nanocages Use Ion Channels, Catalytic Sites, and Nucleation Channels to Manage Iron/Oxygen Chemistry. *Curr. Opin. Chem. Biol.* **2011**, *15*, 304–311.
- (6) Theil, E. C.; Behera, R. K.; Tosh, T. Ferritins for Chemistry and for Life. *Coord. Chem. Rev.* **2013**, *257*, 579–586.
- (7) Watt, R. K. The Many Faces of the Octahedral Ferritin Protein. *Biometals* **2011**, *24*, 489–500.
- (8) Watt, R. K. A Unified Model for Ferritin Iron Loading by the Catalytic Center: Implications for Controlling "Free Iron" During Oxidative Stress. *ChemBioChem* **2013**, *14*, 415–419.
- (9) Zhao, G. H.; Arosio, P.; Chasteen, N. D. Iron(II) and Hydrogen Peroxide Detoxification by Human H-Chain Ferritin. An EPR Spin-Trapping Study. *Biochemistry* **2006**, *45*, 3429–3436.
- (10) Yamashita, I.; Iwahori, K.; Kumagai, S. Ferritin in the Field of Nanodevices. *Biochim. Biophys. Acta, Gen. Subj.* **2010**, *1800*, 846–857.
- (11) Zhen, Z.; Tang, W.; Guo, C.; Chen, H.; Lin, X.; Liu, G.; Fei, B.; Chen, X.; Xu, B.; Xie, J. Ferritin Nanocages to Encapsulate and Deliver Photosensitizers for Efficient Photodynamic Therapy against Cancer. *ACS Nano* **2013**, *7*, 6988–6996.
- (12) Kasyutich, O.; Ilari, A.; Fiorillo, A.; Tatchev, D.; Hoell, A.; Ceci, P. Silver Ion Incorporation and Nanoparticle Formation inside the Cavity of Pyrococcus Furiosus Ferritin: Structural and Size-Distribution Analyses. *J. Am. Chem. Soc.* **2010**, *132*, 3621–3627.
- (13) May, C. A.; Grady, J. K.; Laue, T. M.; Poli, M.; Arosio, P.; Chasteen, N. D. The Sedimentation Properties of Ferritins. New Insights and Analysis of Methods of Nanoparticle Preparation. *Biochim. Biophys. Acta, Gen. Subj.* **2010**, *1800*, 858–870.
- (14) Polanams, J.; Ray, A. D.; Watt, R. K. Nanophase Iron Phosphate, Iron Arsenate, Iron Vanadate, and Iron Molybdate Minerals Synthesized within the Protein Cage of Ferritin. *Inorg. Chem.* **2005**, *44*, 3203–3209.
- (15) Harada, T.; Yoshimura, H. Ferritin Protein Encapsulated Photoluminescent Rare Earth Nanoparticle. *J. Appl. Phys.* **2013**, *114*, 044309–1–044309–8.
- (16) Kang, Y. J.; Uchida, M.; Shin, H. H.; Douglas, T.; Kang, S. Biomimetic Fept Nanoparticle Synthesis within Pyrococcus Furiosus Ferritins and Their Layer-by-Layer Formation. *Soft Matter* **2011**, *7*, 11078–11081.
- (17) Keyes, J. D.; Hilton, R. J.; Farrer, J.; Watt, R. K. Ferritin as a Photocatalyst and Scaffold for Gold Nanoparticle Synthesis. *J. Nanopart. Res.* **2011**, *13*, 2563–2575.
- (18) Kim, J. W.; Posey, A. E.; Watt, G. D.; Choi, S. H.; Lillehei, P. T. Gold Nanoshell Assembly on a Ferritin Protein Employed as a Bio-Template. *J. Nanosci. Nanotechnol.* **2010**, *10*, 1771–1777.
- (19) Zheng, B.; Uenuma, M.; Okamoto, N.; Honda, R.; Ishikawa, Y.; Uraoka, Y.; Yamashita, I. Construction of Au Nanoparticle/Ferritin Satellite Nanostructure. *Chem. Phys. Lett.* **2012**, *547*, 52–57.
- (20) Kim, J.-W.; Choi, S. H.; Lillehei, P. T.; Chu, S.-H.; King, G. C.; Watt, G. D. Electrochemically Controlled Reconstitution of Immobilized Ferritins for Bioelectronic Applications. *J. Electroanal. Chem.* **2007**, *601*, 8–16.
- (21) Yuan, Z.; Petsev, D. N.; Prevo, B. G.; Velev, O. D.; Atanassov, P. Two-Dimensional Nanoparticle Arrays Derived from Ferritin Monolayers. *Langmuir* **2007**, *23*, 5498–5504.
- (22) Zhang, F.; Gates, R. J.; Smentkowski, V. S.; Natarajan, S.; Gale, B. K.; Watt, R. K.; Asplund, M. C.; Linford, M. R. Direct Adsorption and Detection of Proteins, Including Ferritin, onto Microlens Array Patterned Bioarrays. *J. Am. Chem. Soc.* **2007**, *129*, 9252–9253.
- (23) Shin, K. M.; Watt, R. K.; Watt, G. D.; Choi, S. H.; Kim, H.-H.; Kim, S. I.; Kim, S. J. Characterization of Ferritin Core on Redox Reactions as a Nanocomposite for Electron Transfer. *Electrochim. Acta* **2010**, *55*, 3486–3490.
- (24) Zhang, B.; Harb, J. N.; Davis, R. C.; Choi, S.; Kim, J. W.; Miller, T.; Chu, S. H.; Watt, G. D. Electron Exchange between  $\text{Fe}(\text{II})$ -Horse Spleen Ferritin and  $\text{Co}(\text{III})/\text{Mn}(\text{III})$  Reconstituted Horse Spleen and Azotobacter Vinelandii Ferritins. *Biochemistry* **2006**, *45*, 5766–5774.
- (25) Crichton, R. R.; Declercq, J. P. X-Ray Structures of Ferritins and Related Proteins. *Biochim. Biophys. Acta, Gen. Subj.* **2010**, *1800*, 706–718.
- (26) Hempstead, P. D.; Yewdall, S. J.; Fernie, A. R.; Lawson, D. M.; Artymiuk, P. J.; Rice, D. W.; Ford, G. C.; Harrison, P. M. Comparison of the Three-Dimensional Structures of Recombinant Human H and Horse L Ferritins at High Resolution. *J. Mol. Biol.* **1997**, *268*, 424–448.
- (27) Bertini, I.; Lalli, D.; Mangani, S.; Pozzi, C.; Rosa, C.; Theil, E. C.; Turano, P. Structural Insights into the Ferroxidase Site of Ferritins from Higher Eukaryotes. *J. Am. Chem. Soc.* **2012**, *134*, 6169–6176.
- (28) Zhao, G. H.; Su, M. H.; Chasteen, N. D. Mu-1,2-1-Peroxo Diferric Complex Formation in Horse Spleen Ferritin. A Mixed H/L-Subunit Heteropolymer. *J. Mol. Biol.* **2005**, *352*, 467–477.
- (29) Theil, E. C.; Matzapetakis, M.; Liu, X. F. Ferritins: Iron/Oxygen Biominerals in Protein Nanocages. *J. Biol. Inorg. Chem.* **2006**, *11*, 803–810.
- (30) Turano, P.; Lalli, D.; Felli, I. C.; Theil, E. C.; Bertini, I. Nmr Reveals Pathway for Ferric Mineral Precursors to the Central Cavity of Ferritin. *Proc. Natl. Acad. Sci. U. S. A.* **2010**, *107*, 545–550.
- (31) Liu, X. S.; Patterson, L. D.; Miller, M. J.; Theil, E. C. Peptides Selected for the Protein Nanocage Pores Change the Rate of Iron Recovery from the Ferritin Mineral. *J. Biol. Chem.* **2007**, *282*, 31821–31825.
- (32) Theil, E. C.; Liu, X. F. S.; Tosh, T. Gated Pores in the Ferritin Protein Nanocage. *Inorg. Chim. Acta* **2008**, *361*, 868–874.
- (33) Tosh, T.; Ng, H.-L.; Bhattacharjee, O.; Alber, T.; Theil, E. C. Moving Metal Ions through Ferritin-Protein Nanocages from Three-Fold Pores to Catalytic Sites. *J. Am. Chem. Soc.* **2010**, *132*, 14562–14569.
- (34) Tosh, T.; Behera, R. K.; Theil, E. C. Ferritin Ion Channel Disorder Inhibits  $\text{Fe}(\text{II})/\text{O}_2$  Reactivity at Distant Sites. *Inorg. Chem.* **2012**, *51*, 11406–11411.

- (35) Treffry, A.; Bauminger, E. R.; Hechel, D.; Hodson, N. W.; Nowik, I.; Yewdall, S. J.; Harrison, P. M. Defining the Roles of the Threefold Channels in Iron Uptake, Iron Oxidation and Iron-Core Formation in Ferritin - a Study Aided by Site-Directed Mutagenesis. *Biochem. J.* **1993**, *296*, 721–728.
- (36) d'Estaintot, B. L.; Paolo, S.; Granier, T.; Gallois, B.; Chevalier, J. M.; Precigoux, G.; Levi, S.; Arosio, P. Crystal Structure and Biochemical Properties of the Human Mitochondrial Ferritin and Its Mutant Ser144ala. *J. Mol. Biol.* **2004**, *340*, 277–293.
- (37) Toussaint, L.; Bertrand, L.; Hue, L.; Crichton, R. R.; Declercq, J. P. High-Resolution X-Ray Structures of Human Apoferritin H-Chain Mutants Correlated with Their Activity and Metal-Binding Sites. *J. Mol. Biol.* **2007**, *365*, 440–452.
- (38) Haldar, S.; Bevers, L. E.; Toshia, T.; Theil, E. C. Moving Iron through Ferritin Protein Nanocages Depends on Residues Throughout Each Four Alpha-Helix Bundle Subunit. *J. Biol. Chem.* **2011**, *286*, 25620–25627.
- (39) Barnes, C. M.; Theil, E. C.; Raymond, K. N. Iron Uptake in Ferritin Is Blocked by Binding of  $[Cr(Tren)(H_2O)(OH)]^{2+}$ ; a Slow Dissociating Model for  $[Fe(H_2O)_6]^{2+}$ . *Proc. Natl. Acad. Sci. U. S. A.* **2002**, *99*, 5195–5200.
- (40) Liu, X. F.; Jin, W. L.; Theil, E. C. Opening Protein Pores with Chaotropes Enhances Fe Reduction and Chelation of Fe from the Ferritin Biomineral. *Proc. Natl. Acad. Sci. U. S. A.* **2003**, *100*, 3653–3658.
- (41) Jin, W. L.; Takagi, H.; Pancorbo, B.; Theil, E. C. “Opening” the Ferritin Pore for Iron Release by Mutation of Conserved Amino Acids at Interhelix and Loop Sites. *Biochemistry* **2001**, *40*, 7525–7532.
- (42) Takagi, H.; Shi, D. S.; Ha, Y.; Allewell, N. M.; Theil, E. C. Localized Unfolding at the Junction of Three Ferritin Subunits - a Mechanism for Iron Release? *J. Biol. Chem.* **1998**, *273*, 18685–18688.
- (43) Ceci, P.; Di Cecca, G.; Falconi, M.; Oteri, F.; Zamparelli, C.; Chiancone, E. Effect of the Charge Distribution Along the “Ferritin-Like” Pores of the Proteins from the Dps Family on the Iron Incorporation Process. *J. Biol. Inorg. Chem.* **2011**, *16*, 869–880.
- (44) Douglas, T.; Ripoll, D. R. Calculated Electrostatic Gradients in Recombinant Human H-Chain Ferritin. *Protein Sci.* **1998**, *7*, 1083–1091.
- (45) Aguilar, C. M.; De Almeida, W. B.; Rocha, W. R. The Electronic Spectrum of  $Fe^{2+}$  Ion in Aqueous Solution: A Sequential Monte Carlo/Quantum Mechanical Study. *Chem. Phys. Lett.* **2007**, *449*, 144–148.
- (46) Behera, R. K.; Ng, H. L.; Bhattachari, O.; Alber, T.; Theil, E. C. Ferritin Protein Nanocage Ion Channels Gating by N-Terminal Extensions. *J. Biol. Chem.* **2012**, *287*, 13016–13025.
- (47) Bou-Abdallah, F.; Zhao, G. H.; Mayne, H. R.; Arosio, P.; Chasteen, N. D. Origin of the Unusual Kinetics of Iron Deposition in Human H-Chain Ferritin. *J. Am. Chem. Soc.* **2005**, *127*, 3885–3893.
- (48) Zhang, B.; Watt, R. K.; Galvez, N.; Dominguez-Vera, J. M.; Watt, G. D. Rate of Iron Transfer through the Horse Spleen Ferritin Shell Determined by the Rate of Formation of Prussian Blue and Fe-Desferrioxamine within the Ferritin Cavity. *Biophys. Chem.* **2006**, *120*, 96–105.
- (49) Bou-Abdallah, F.; Zhao, G.; Biasiotto, G.; Poli, M.; Arosio, P.; Chasteen, N. D. Facilitated Diffusion of Iron(II) and Dioxygen Substrates into Human H-Chain Ferritin. A Fluorescence and Absorbance Study Employing the Ferroxidase Center Substitution Y34W. *J. Am. Chem. Soc.* **2008**, *130*, 17801–17811.
- (50) Laghaei, R.; Evans, D. G.; Coalson, R. D. Metal Binding Sites of Human H-Chain Ferritin and Iron Transport Mechanism to the Ferroxidase Sites: A Molecular Dynamics Simulation Study. *Proteins: Struct., Funct., Bioinf.* **2013**, *81*, 1042–1050.
- (51) Eisenberg, R. S. Computing the Field in Proteins and Channels. *J. Membr. Biol.* **1996**, *150*, 1–25.
- (52) Coalson, R. D.; Kurnikova, M. G. Poisson-Nernst-Planck Theory of Ion Permeation through Biological Channels. In *Biological and Medical Physics, Biomedical Engineering*; Chung, S. H., Andersen, O. S., Krishnamurthy, V., Eds.; Springer: New York, 2007; pp 449–484.
- (53) Hilton, R. J.; Zhang, B.; Martineau, L. N.; Watt, G. D.; Watt, R. K. Anion Deposition into Ferritin. *J. Inorg. Biochem.* **2012**, *108*, 8–14.
- (54) Phillips, J. C.; Braun, R.; Wang, W.; Gumbart, J.; Tajkhorshid, E.; Villa, E.; Chipot, C.; Skeel, R. D.; Kale, L.; Schulten, K. Scalable Molecular Dynamics with Namd. *Comput. Chem.* **2005**, *26*, 1781–1802.
- (55) MacKerrell, A. D. J.; Brooks, B.; Brooks, C. L. I.; Nilsson, L.; Roux, B.; Won, Y.; Karplus, M. *Charmm: The Energy Function and Its Parameterization with an Overview of the Program*; John Wiley & Sons: Chichester, U.K., 1998; Vol. 1.
- (56) Humphrey, W.; Dalke, A.; Schulter, K. VMD - Visual Molecular Dynamics. *J. Mol. Graphics* **1996**, *14*, 33–38.
- (57) DeLano, W. L. *The PyMOL Molecular Graphics System*, Version 1.3rl; Schrödinger, LLC: New York, 2010.
- (58) Smart, O. S.; Neduvilil, J. G.; Wang, X.; Wallace, B. A.; Sansom, M. S. Hole: A Program for the Analysis of the Pore Dimensions of Ion Channel Structural Models. *J. Mol. Graphics* **1996**, *14*, 354–360.
- (59) Roux, B.; Karplus, M. Ion Transport in a Gramicidin-Like Channel: Dynamics and Mobility. *J. Phys. Chem.* **1991**, *95*, 4856–4868.
- (60) Straub, J. E.; Borkovec, M.; Berne, B. J. Calculation of Dynamic Friction on Intramolecular Degrees of Freedom. *J. Phys. Chem.* **1987**, *91*, 4995–4998.
- (61) Koneshan, S.; Lynden-Bell, R. M.; Rasaiah, J. C. Friction Coefficients of Ions in Aqueous Solution at  $25^{\circ}\text{C}$ . *J. Am. Chem. Soc.* **1998**, *120*, 12041–12050.
- (62) Kubo, R. *Many-Body Theory*; Syokabo and Benjamin: Tokyo, 1966.
- (63) Chandrasekhar, S. Stochastic Problems in Physics and Astronomy. *Rev. Mod. Phys.* **1943**, *15*, 1–89.
- (64) Kurnikova, M. G.; Coalson, R. D.; Graf, P.; Nitzan, A. A Lattice Relaxation Algorithm for Three-Dimensional Poisson-Nernst-Planck Theory with Application to Ion Transport through the Gramicidin a Channel. *Biophys. J.* **1999**, *76*, 642–656.
- (65) Baker, N. A.; Sept, D.; S., J.; Holst, M. J.; McCammon, J. A. Electrostatics of Nanosystems: Application to Microtubules and the Ribosome. *Proc. Natl. Acad. Sci. U. S. A.* **2001**, *98*, 10037–10041.
- (66) Cheng, M. H.; Coalson, R. D.; Tang, P. Molecular Dynamics and Brownian Dynamics Investigation of Ion Permeation and Anesthetic Halothane Effects on a Proton-Gated Ion Channel. *J. Am. Chem. Soc.* **2010**, *132*, 16442–16449.
- (67) Mamonov, A. B.; Kurnikova, M. G.; Coalson, R. D. Diffusion Constant of  $K^+$  inside Gramicidin A: A Comparative Study of Four Computational Methods. *Biophys. Chem.* **2006**, *124*, 268–278.
- (68) CRC Handbook of Chemistry and Physics; CRC Press: Cleveland, OH, 1994.
- (69) Passiniemi, P. Accurate Tracer Diffusion Coefficients of  $\text{Na}^+$  and  $\text{Cl}^-$  Ions in Dilute Aqueous Sodium Chloride Solutions Measured with the Closed Capillary Method. *J. Solution Chem.* **1983**, *12*, 801–813.
- (70) Treffry, A.; Harrison, P. M. Spectroscopic Studies on the Binding of Iron, Terbium, and Zinc by Apoferritin. *J. Inorg. Biochem.* **1984**, *21*, 9–20.
- (71) Wardeska, J. G.; Viglione, B.; Chasteen, N. D. Metal Ion Complexes of Apoferritin. Evidence for Initial Binding in the Hydrophilic Channels. *J. Biol. Chem.* **1986**, *261*, 6677–6683.
- (72) Paques, E. P.; Pagès, A.; Chrilton, R. R. A Kinetic Study of the Mechanism of Ferritin Formation: The Effects of Buffer, of Ph, and of the Iron Content of the Molecule. *J. Mol. Catal.* **1868**, *5*, 363–375.
- (73) Yang, X.; Chasteen, N. D. Molecular Diffusion into Horse Spleen Ferritin: A Nitroxide Radical Spin Probe Study. *Biophys. J.* **1996**, *71*, 1587–1595.
- (74) Cardenas, A. E.; Coalson, R. D.; Kurnikova, M. G. Three-Dimensional Poisson-Nernst-Planck Theory Studies: Influence of Membrane Electrostatics on Gramicidin a Channel Conductance. *Biophys. J.* **2000**, *79*, 80–93.
- (75) Mamonov, A. B.; Coalson, R. D.; Nitzan, A.; Kurnikova, M. G. The Role of the Dielectric Barrier in Narrow Biological Channels: A Novel Composite Approach to Modeling Single-Channel Currents. *Biophys. J.* **2003**, *84*, 3646–3661.

- (76) Noskov, S. Y.; Im, W.; Roux, B. Ion Permeation through the Alpha-Hemolysin Channel: Theoretical Studies Based on Brownian Dynamics and Poisson-Nerst-Planck Electrodiffusion Theory. *Biophys. J.* **2004**, *87*, 2299–2309.
- (77) Hollerbach, U.; Chen, D. P.; Busath, D. D.; Eisenberg, B. Predicting Function from Structure Using the Poisson-Nernst-Planck Equations: Sodium Current in the Gramicidin a Channel. *Langmuir* **2000**, *16*, 5509–5514.
- (78) Choudhary, O. P.; Ujwal, R.; Kowallis, W.; Coalson, R.; Abramson, J.; Grabe, M. The Electrostatics of Vdac: Implications for Selectivity and Gating. *J. Mol. Biol.* **2010**, *396*, 580–592.
- (79) Breuer, W.; Epsztejn, S.; Cabantchik, Z. I. Iron Acquired from Transferrin by K562 Cells Is Delivered into a Cytoplasmic Pool of Chelatable Iron(II). *J. Biol. Chem.* **1995**, *270*, 24209–24215.
- (80) Aksimentiev, A.; Schulten, K. Imaging  $\alpha$ -Hemolysin with Molecular Dynamics: Ionic Conductance, Osmotic Permeability, and the Electrostatic Potential Map. *Biophys. J.* **2005**, *88*, 3745–3761.
- (81) Kutzner, C.; Grubmuller, H.; de Groot, B. L.; Zachariae, U. Computational Electrophysiology: The Molecular Dynamics of Ion Channel Permeation and Selectivity in Atomistic Detail. *Biophys. J.* **2011**, *101*, 809–817.
- (82) Allen, T. W.; Hoyles, M.; Kuyucak, S.; Chung, S. H. Molecular and Brownian Dynamics Study of Ion Selectivity and Conductivity in the Potassium Channel. *Chem. Phys. Lett.* **1999**, *313*, 358–365.
- (83) Graf, P.; Nitzan, A.; Kurnikova, M. G.; Coalson, R. D. A Dynamic Lattice Monte Carlo Model of Ion Transport in Inhomogeneous Dielectric Environments: Method and Implementations. *J. Phys. Chem. B* **2000**, *104*, 12324–12338.
- (84) Cheng, M. H.; Mamonov, A.; Dukes, J. W.; Coalson, R. D. Modeling the Fast Gating Mechanism in ClC-0 Chloride Channels. *J. Phys. Chem. B* **2007**, *111*, 5956–5965.
- (85) Coalson, R. D.; Cheng, M. H. Discrete-State Representation of Ion Permeation Coupled to Fast Gating in a Model of ClC Chloride Channels: Comparison to Multi-Ion Continuous Space Brownian Dynamics Simulations. *J. Phys. Chem. B* **2010**, *114*, 1424–1433.
- (86) Theil, E. C. Ferritin: The Protein Nanocage and Iron Biomimetic in Health and in Disease. *Inorg. Chem.* **2013**, *52*, 12223–12233.
- (87) Funk, F.; Lenders, J. P.; Crichton, R. R.; Schneider, W. Reductive Mobilisation of Ferritin Iron. *Eur. J. Biochem.* **1985**, *52*, 167–172.
- (88) Toshia, T.; Behera, R. K.; Ng, H.-L.; Bhattacharjee, O.; Alber, T.; Theil, E. C. Ferritin Protein Nanocage Ion Channels: Gating by N-Terminal Extensions. *J. Biol. Chem.* **2012**, *287*, 13016–13025.
- (89) Duncan, A.; Sedgewick, R. D.; Coalson, R. D. Improved Local Lattice Approach for Coulombic Simulations. *Phys. Rev. E* **2005**, *71*, 046702–1–046702–8.
- (90) Guldbrand, L.; Jönsson, B.; Wennerström, H.; Linse, P. Electrical Double Layer Forces. A Monte Carlo Study. *J. Chem. Phys.* **1984**, *80*, 2221–2228.